OPEN ACCESS Freely available online

PLOS ONE

Multi-Scale Characterization of Lyotropic Liquid Crystals Using ^{2}H and Diffusion MRI with Spatial Resolution in Three Dimensions

Diana Bernin[1,2], Vanessa Koch[4], Magnus Nydén[3], Daniel Topgaard[4]*

1 Applied Surface Chemistry, Chalmers University of Technology, Gothenburg, Sweden, **2** Swedish NMR Centre, University of Gothenburg, Gothenburg, Sweden, **3** Ian Wark Research Institute, University of South Australia, Adelaide, South Australia, Australia, **4** Division of Physical Chemistry, Department of Chemistry, Lund University, Lund, Sweden

Abstract

The ability of lyotropic liquid crystals to form intricate structures on a range of length scales can be utilized for the synthesis of structurally complex inorganic materials, as well as in devices for controlled drug delivery. Here we employ magnetic resonance imaging (MRI) for non-invasive characterization of nano-, micro-, and millimeter scale structures in liquid crystals. The structure is mirrored in the translational and rotational motion of the water, which we assess by measuring spatially resolved self-diffusion tensors and ^{2}H spectra. Our approach differs from previous works in that the MRI parameters are mapped with spatial resolution in all three dimensions, thus allowing for detailed studies of liquid crystals with complex millimeter-scale morphologies that are stable on the measurement time-scale of 10 hours. The ^{2}H data conveys information on the nanometer-scale structure of the liquid crystalline phase, while the combination of diffusion and ^{2}H data permits an estimate of the orientational distribution of micrometer-scale anisotropic domains. We study lamellar phases consisting of the nonionic surfactant $C_{10}E_3$ in ^2H_2O, and follow their structural equilibration after a temperature jump and the cessation of shear. Our experimental approach may be useful for detailed characterization of liquid crystalline materials with structures on multiple length scales, as well as for studying the mechanisms of phase transitions.

Citation: Bernin D, Koch V, Nydén M, Topgaard D (2014) Multi-Scale Characterization of Lyotropic Liquid Crystals Using ^{2}H and Diffusion MRI with Spatial Resolution in Three Dimensions. PLoS ONE 9(6): e98752. doi:10.1371/journal.pone.0098752

Editor: Dariush Hinderberger, Martin-Luther-Universität Halle-Wittenberg, Germany

Received January 17, 2014; **Accepted** May 7, 2014; **Published** June 6, 2014

Funding: This work is funded by VINNOVA through the VINN Excellence Centre SuMo Biomaterials (Supramolecular Biomaterials - Structure dynamics and properties) and the Swedish Research Council VR (grant numbers 2009–6794 and 2011–4334). The funders had no role in study design, data collection and analysis, decision to publish, or preparation of the manuscript.

Competing Interests: The authors have declared that no competing interests exist.

* E-mail: daniel.topgaard@fkem1.lu.se

Introduction

Amphiphilic molecules such as surfactants and lipids spontaneously form a range of liquid crystalline phases when mixed with water [1,2]. While the nanometer-scale structure is dictated by the temperature and the local chemical composition, the morphology on larger length scales is highly tunable through, e.g., the thermal history [3], the presence of magnetic fields [4–7], or the application of shear [8–14]. Micrometer-scale structures such as multi-lamellar vesicles (MLVs) are of interest as microreactors [15] and for drug-delivery applications [16], while the millimeter-scale organization is relevant when the liquid crystalline phase is used as a template for inorganic materials [17,18]. After removing the sources of the perturbations, the formed superstructures are not at true thermodynamic equilibrium, but they may nevertheless be metastable for extended periods of time and useful for practical applications.

The interface between the water and the hydrophobic core of the surfactant aggregates imparts anisotropy to the rotational and translational motion of the water molecules. Although the orientational ordering of the water is minuscule, it can be detected through the exquisitely sensitive ^{2}H quadrupolar interaction using nuclear magnetic resonance (NMR) spectroscopy [19]. Not only can ^{2}H NMR be used for distinguishing between cubic, hexagonal, and lamellar liquid crystalline phases [20,21], but also for determining the degree of orientational order [4–7], as well as the size [22–26] of the anisotropic microcrystallites. The features of the ^{2}H spectrum are sensitive to the orientation of the liquid crystalline phase with respect to the direction of the applied external magnetic field. For axially symmetric phases, e.g., hexagonal and lamellar, the angle between the magnetic field and the main symmetry axis of the phase determines the observed ^{2}H spectrum. Conversely, there is no information about the orientation within the plane perpendicular to the magnetic field, thus making it difficult to pinpoint the exact microcrystallite orientation in 3D space.

The translational diffusion of water is conveniently monitored with pulsed-gradient spin-echo (PGSE) NMR [27–29], in which the ^{1}H NMR signal is encoded for molecular displacements using magnetic field gradients. Just as for ^{2}H spectroscopy, the degree and length scale of the orientational ordering of the anisotropic microcrystallites can be determined using PGSE methods [30–33]. Modern NMR spectrometers usually have the capability of generating field gradients in three orthogonal directions, thus making it possible to determine the full diffusion tensor from which

the preferred direction of microcrystallite orientation can be estimated [27,34,35].

Using magnetic resonance imaging (MRI) methods, both ^{2}H spectroscopy [36] and diffusion experiments [37,38] can be performed in a spatially resolved manner. In the context of surfactant science, the spatial resolution has often been limited to a single dimension [39–41], with two examples of two-dimensional mapping of diffusion tensors [42,43]. Combined one-dimensional mapping of ^{2}H spectra and diffusion coefficients has been used to investigate transitions between various lamellar phase morphologies induced by the application of shear and temperature cycling [26,40].

In this work, we investigate the benefit of full three-dimensional mapping of diffusion tensors and ^{2}H spectra for characterizing hierarchically organized liquid crystalline phases with intricate structures on the millimeter scale. As a model system we use the non-ionic surfactant triethylene glycol monodecyl ether ($C_{10}E_3$) and deuterated water (^2H_2O), which has often been applied in studies of lamellar phase morphologies [13,23,24,26,33,40,43,44]. Structures on a wide range of length scales are assessed by correlating the complementary information from diffusion tensors and ^{2}H spectra imaged at sub-millimeter spatial resolution. On the time-scale of days and weeks, we follow the breakdown of MLVs after the cessation of shear and the formation of a uniformly oriented lamellar phase after a temperature quench, thereby obtaining structural information at an unprecedented level of detail. In addition to the time-dependence of the bulk phase composition during a phase transition, which is often analyzed with the Johnson-Mehl-Avrami-Kolmogorov model [45,46], our approach also allows for identification of the nucleation sites and the three-dimensional growth pattern of the new phase.

Methods

Theoretical considerations

In this section we first briefly review the theoretical basis for ^{2}H NMR spectroscopy and diffusion tensor imaging (DTI), and subsequently show schematic results that can be expected for typical micrometer-scale morphologies of lamellar phases.

^{2}H NMR. The ^{2}H nucleus has a spin quantum number $I=1$ and an electric quadrupole moment, resulting in an NMR spectrum dominated by the interactions between the quadrupole moment and electric field gradients. For ^2H_2O in an isotropic liquid, the quadrupolar interaction is averaged to zero by molecular motion and the ^{2}H spectrum consists of a single sharp peak. Conversely, the preferential molecular orientation in an anisotropic liquid leads to a spectrum consisting of a doublet with splitting $\Delta\nu_Q$ given by [47,48]

$$\Delta\nu_Q = \frac{3}{2}\chi\overline{P_2(\cos\theta)}, \tag{1}$$

where $P_2(x)=(3x^2-1)/2$ is the second Legendre polynomial, θ is the angle between the magnetic field and the O-^{2}H bond vector, and χ is the quadrupole coupling constant given by

$$\chi = \frac{e^2qQ}{h}, \tag{2}$$

where e is the unit charge, h is the Planck constant, eq is the electric field gradient along the O-^{2}H bond axis, and Q is the nuclear quadrupole moment. The value of χ is 254 kHz for water at 25°C [49]. The overline in Eq. 1 indicates an average over fluctuations of θ that occur much faster than the inverse strength of the interaction χ. In anisotropic liquid crystals, the molecular motion is symmetric with respect to the phase director inclined at a polar angle α from the magnetic field. Assuming that the molecules remain in a domain with uniform value of α during the χ time scale, then Eq. 1 can be expressed as [50]

$$\Delta\nu_Q(\alpha) = \frac{3}{2}\chi S P_2(\cos\alpha), \tag{3}$$

where the order parameter S is given by

$$S = \overline{P_2(\cos\theta_\alpha)}, \tag{4}$$

and θ_α is the angle between the bond axis and the director. For water in typical surfactant lamellar phases, Eq. 4 evaluates to approximately 0.01, leading to observed quadrupolar splittings on the order of 1 kHz.

Lyotropic liquid crystals usually consist of an ensemble of randomly oriented anisotropic domains. The resulting powder-pattern ^{2}H spectrum $I_P(\nu)$ can be written as

$$I_P(\nu) = \int_0^{\pi/2} P(\alpha)\mathfrak{L}_d(\nu,\nu_0\pm 0.5\Delta\nu_Q(\alpha),R)\,d\alpha, \tag{5}$$

where $P(\alpha)$ is the probability density of angles α, normalized in the interval $0<\alpha<\pi/2$, and $\mathfrak{L}_d(\nu,\nu_0\pm 0.5\Delta\nu_Q(\alpha),R)$ is a Lorentzian doublet lineshape function with peaks of width R centered at the frequencies $\nu=\nu_0\pm 0.5\Delta\nu_Q(\alpha)$. A random distribution of domain orientations in three dimensions corresponds to

$$P(\alpha) = \sin\alpha. \tag{6}$$

The effect of preferential alignment in the magnetic field can be approximated by

$$P(\alpha) = \frac{\sin\alpha e^{-W\cos\alpha}}{Z}, \tag{7}$$

where W is a weighting parameter, corresponding to the degree of alignment, and Z is a normalization factor assuring that $\int_0^{\pi/2} P(\alpha)\,d\alpha = 1$. The 3D powder case in Eq. 6 is recovered when $W=0$. Complete alignment at $\alpha=0$ or $\pi/2$ is obtained as W approaches ∞ or $-\infty$, respectively.

Translational diffusion along the curved water layers in multilamellar vesicles (MLVs) may result in molecular reorientation on the millisecond time-scale of the rotationally averaged quadrupolar coupling, giving rise to nuclear relaxation and line broadening. As a consequence, the ^{2}H spectrum features a singlet with a linewidth that is proportional to the square of the MLV radius [24,44]. The lineshape can in this case be approximated by

$$I_{MLV}(\nu) = \mathfrak{L}_s(\nu,\nu_0,R), \tag{8}$$

where $\mathfrak{L}_s(\nu,\nu_0,R)$ is a Lorentzian singlet with width R and centered at $\nu=\nu_0$.

For the purpose of visualizing ^{2}H MRI data, it is useful to extract scalar parameters that describe the experimentally determined spectrum $I(\nu)$. Here, we use the peak area A, the first moment M_1, and the second moment M_2:

$$A = \int_{-\infty}^{\infty} I(v)\,dv, \tag{9}$$

$$M_1 = \frac{1}{A}\int_{-\infty}^{\infty} vI(v)\,dv, \tag{10}$$

and

$$M_2 = \frac{1}{A}\int_{-\infty}^{\infty} (v-M_1)^2 I(v)\,dv. \tag{11}$$

Diffusion tensor imaging (DTI). Translational diffusion in a homogeneous and anisotropic medium can be described with the second rank diffusion tensor $\mathbf{D}$, which is determined by its eigenvalues λ_1, λ_2, and λ_3 ($\lambda_1 \geq \lambda_2 \geq \lambda_3$) as well as the orientation of its eigenvectors with respect to the laboratory coordinate system (x,y,z). The transformation from the principal axis system (PAS) of the diagonalized diffusion tensor $\mathbf{D}^{\mathrm{PAS}}$ to the lab frame is brought about by

$$\boldsymbol{D} = \mathbf{R}\mathbf{D}^{\mathrm{PAS}}\mathbf{R}^{-1}, \tag{12}$$

where $\mathbf{R}$ is a rotation matrix given by the three Euler angles.

In the pulsed-gradient spin-echo (PGSE) pulse sequence, the NMR signal is encoded for diffusion using two magnetic field gradient pulses of duration δ, amplitude G, direction $\hat{\mathbf{G}}$, and time lapse between the leading edges Δ. The detected signal intensity I is expressed as

$$\frac{I}{I_0} = \exp\left(-b\hat{\mathbf{G}}\cdot\mathbf{D}\cdot\hat{\mathbf{G}}\right), \tag{13}$$

where I_0 is the signal intensity at $G=0$ and the diffusion weighting variable b is given by

$$b = \gamma^2\delta^2G^2(\Delta-\delta/3), \tag{14}$$

where γ is the magnetogyric ratio. The scalar products in Eq. 13 can be explicitly written as

$$\hat{\mathbf{G}}\cdot\mathbf{D}\cdot\hat{\mathbf{G}} = \hat{G}_x^2D_{xx} + \hat{G}_y^2D_{yy} + \hat{G}_z^2D_{zz} + 2\hat{G}_x\hat{G}_yD_{xy} + 2\hat{G}_x\hat{G}_zD_{xz} + 2\hat{G}_y\hat{G}_zD_{yz}.$$

Experimentally, the diffusion tensor $\mathbf{D}$ is estimated by analyzing the diffusional signal decay recorded for a series of b-values and gradient directions $\hat{\mathbf{G}}$ [51–53].

There are many ways to visualize the diffusion tensors, e.g., by plotting arrays of diffusion ellipsoids [34] or superquadrics [51,54]. Alternatively, one can extract rotationally invariant indices such as the mean diffusivity (MD)

$$\mathrm{MD} = \frac{\lambda_1+\lambda_2+\lambda_3}{3} \tag{16}$$

and the fractional anisotropy (FA) [55,56]

$$\mathrm{FA} = \frac{\sqrt{(\lambda_1-\lambda_2)^2+(\lambda_2-\lambda_3)^2+(\lambda_3-\lambda_1)^2}}{\sqrt{2}\sqrt{\lambda_1^2+\lambda_3^2+\lambda_3^2}}, \tag{17}$$

as well as the linear (CL) and planar (CP) measures [57]

$$\mathrm{CL} = \frac{\lambda_1-\lambda_2}{\lambda_1} \tag{18}$$

and

$$\mathrm{CP} = \frac{\lambda_2-\lambda_3}{\lambda_1}. \tag{19}$$

^{2}H NMR, DTI, and lamellar phase morphology. Surfactant/water lamellar phases can have a range of different morphologies on length scales above micrometers, e.g., uniformly or randomly oriented microdomains and multi-lamellar vesicles (MLVs). As illustrated with the schematic NMR data in Fig. 1, neither diffusion tensors nor ^{2}H spectra are by themselves sufficient to unambiguously determine the microstructure. Still, all the different cases can be distinguished by combining the information from the two NMR modalities.

For a lamellar phase oriented with the director along x or y, shown in Figs. 1 (a) and (b), the ^{2}H spectrum features a doublet split by $\Delta\nu_{\mathrm{Q}}(\alpha)$. Noteworthily, there is no difference in the degree of splitting for single domain lamellar phases aligned with the magnetic field but rotated in the plane perpendicular to the magnetic field since the angle α remains constant. Conversely, the orientation of the diffusion tensors directly mirror the orientation of the lamellae. Assuming $\lambda_1=\lambda_2\gg\lambda_3$, the values of the rotationally invariant diffusion tensor indices are given by $\mathrm{FA}=1/\sqrt{2}$, $\mathrm{CL}=0$, and $\mathrm{CP}=1$ for all cases (a)-(c), while the lab-frame diffusion tensor elements D_{xx}, D_{yy}, and D_{zz} differ. The case with the lamellar director along z displays twice as large quadrupolar splitting as the x and y cases on account of the factor $P_2(\cos\alpha)$ in the expression for $\Delta\nu_{\mathrm{Q}}(\alpha)$ in Eq. 3.

A spread of domain orientations most often results in ^{2}H powder line shapes [58] as illustrated in Figs. 1 (e)-(g), the only exception being if the different domains happen to have same angle α with respect to the magnetic field as shown in Fig. 1 (d). This seemingly unlikely case nevertheless appears quite often when the domains are in the presence of an aligning magnetic field. The diffusion tensors have cylindrical shapes for all the two-dimensional powders in Figs. 1 (d)-(f) despite the fact that the underlying compartment geometry is planar. The diffusion tensor indices evaluate to $\mathrm{FA}=1/\sqrt{6}$, $\mathrm{CL}=1/2$, and $\mathrm{CP}=0$.

The three-dimensional powder in Fig. 1 (g) results in a ^{2}H powder line shape with characteristic "horns" and "shoulders", while the diffusion tensor shows a spherical symmetry with $\mathrm{FA}=\mathrm{CL}=\mathrm{CP}=0$. Diffusion along the curved water layers in the MLVs results in a ^{2}H spectrum with a broad singlet rather than a doublet [24], see Fig. 1 (h). Isotropic diffusion tensors are obtained for both MLVs and 3D powders, the latter giving higher values of the mean diffusivity.

When several morphologies are present in the sample, the observed ^{2}H spectrum is a superposition of the line shapes from all constituents. An example with coexistence between the 3D powder and MLVs is shown in Fig. 1 (i).

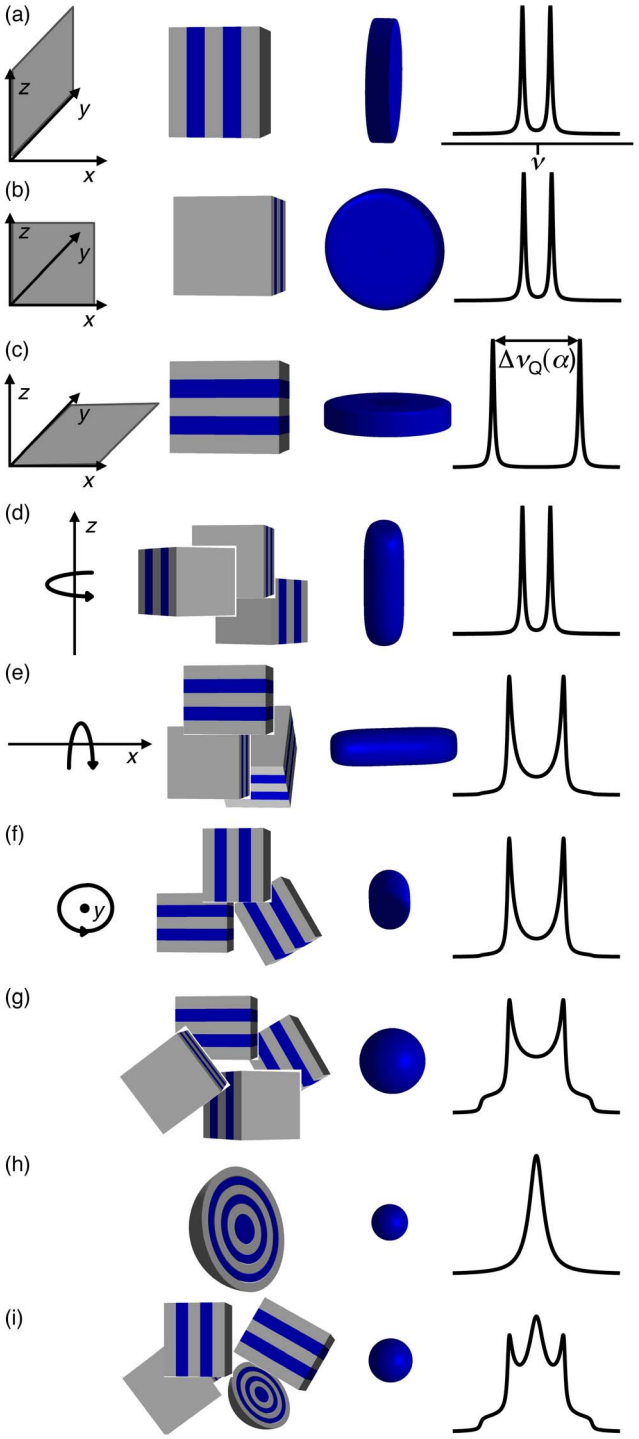

Figure 1. Schematic lamellar phase morphologies with corresponding diffusion tensors and ^{2}H spectra. Column 1: Lab frame coordinate system indicating the direction of domain alignment. The main magnetic field B_0 defines the direction of the z-axis. Column 2: Schematic lamellar phase domains with water and surfactant shown in blue and gray, respectively. Column 3: Diffusion tensors displayed as superquadrics [54]. Column 4: ^{2}H spectra with quadrupolar splitting $\Delta\nu_Q(\alpha)$, see Eq. 3. Rows (a), (b), and (c): Uniform orientation with non-restricted water diffusion in the yz, xz, and xy-planes, respectively. Rows (d), (e), and (f): Domains oriented randomly along the curved arrow with main symmetry axis along z, x, and y-axes, respectively. Row (g): Random orientations in three dimensions. Row (h): Multi-lamellar vesicles (MLVs). Row (i): Mixture of MLVs and randomly oriented domains.
doi:10.1371/journal.pone.0098752.g001

Experimental

Sample preparation. The nonionic surfactant triethylene glycol monodecyl ether, $C_{10}E_3$, (Nikko Chemical Co., Tokyo, Japan) was mixed with deuterated water (Sigma Aldrich, Steinheim, Germany), yielding a final concentration of 40% (w/w) $C_{10}E_3$ and a molar ratio $^2H_2O/C_{10}E_3$ of 24. All chemicals were used without further purification. The concentration of residual protons in the ^2H_2O is sufficient for performing ^{1}H NMR experiments with adequate signal-to-noise ratio. The mixture was equilibrated overnight before being placed in a rheometer (PaarPhysica UDS 200, Hertford, United Kingdom, MK22/M; 1° cone angle). MLVs were formed at 25°C by applying 50 s^{-1} shear until reaching a viscosity plateau after 30–60 min.

After transferring the sample with the help of a syringe into a 5 mm outer diameter NMR tube, the evolution with time was followed by continuous NMR experiments for two weeks. After this set of NMR experiments, the sample was heated to 67°C into a two-phase region with reverse micelles (top) and essentially pure water (bottom) [14]. The temperature was rapidly lowered to 25°C and a second set of NMR experiments was performed for one week. Subsequently, the sample was removed from the magnetic field of the NMR equipment and equilibrated for an additional month at 25°C before a final set of NMR experiments. The combination of the temperature cycle and the presence of a magnetic field results in a uniformly oriented lamellar phase [6].

NMR experiments. NMR experiments were carried out on a Bruker AVII-500 spectrometer operating at ^{1}H and ^{2}H resonance frequencies of 500.13 and 76.77 MHz, respectively. The spectrometer was equipped with a 11.74 T standard bore

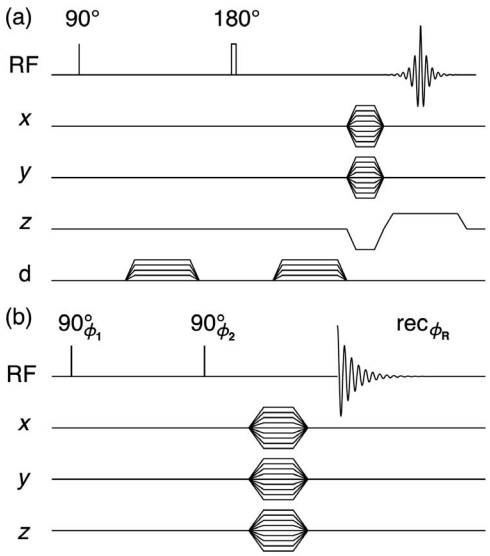

Figure 2. Timing diagrams of the NMR pulse sequences. (a) Diffusion tensor imaging (DTI) pulse sequence based on a ^{1}H spin echo. Spatial resolution is provided by two phase-encoding gradients in the x and y-directions and frequency-encoding gradient in the z-direction, while the diffusion gradients d encode the images for translational motion. The phase and diffusion gradients are incremented independently, yielding a 4D experiment with three spatial and one diffusion dimension. The phase of the 180° RF pulse is cycled in two steps $\pm y$. (b) ^{2}H spectroscopic imaging sequence using a quadrupolar echo and three independently incremented phase-encoding gradients (x,y and z-direction). The sequence yields a 4D data set with three spatial and one spectral dimension. The RF and receiver (rec) phases are cycled in 4 steps according to $\phi_1 = xxyy$, $\phi_2 = y\bar{y}x\bar{x}$, and $\phi_R = xxyy$.
doi:10.1371/journal.pone.0098752.g002

magnet and a MIC-5 probe fitted with a 5 mm $^1H/^2H$ RF insert, allowing for simultaneous ^1H and ^2H studies. All NMR measurements were performed at 25°C.

For the 3D imaging experiments, great care was taken to get exactly the same field of view ($5 \times 5 \times 20$ mm with imaging matrix size $16 \times 16 \times 64$ points) and spatial resolution (isotropic voxels with size 310 μm) for both ^1H and ^2H experiments. One set of NMR experiments lasted 16 h. Gaussian smoothing with 300 μm was applied to the spatial dimensions and an exponential weighting function with 10 Hz to the ^2H spectral dimension. All data processing was performed in Matlab (MathWorks Inc., Massachusetts, USA) using in-house developed code, some of which derives from other sources [59,60].

The DTI pulse sequence in Fig. 2 (a) was used to measure the diffusion tensors with spatial resolution in three dimensions. The signal was acquired at an echo time of 31 ms. Diffusion gradients, with duration $\delta = 10.5$ ms, separation between leading edges $\Delta = 12$ ms, and amplitudes $G = 0.12$ and 0.87 Tm^{-1}, were applied in seven gradient directions: (1,0,0), (0,1,0), (0,0,1), (1,1,0), (1,0,1), (0,1,1), and (1,1,1). Combined with two measurements at $G = 0$, the two gradient amplitude increments and seven directions give a total of 16 gradient combinations in the diffusion dimension. Signal averaging over 2 scans and a recycle delay of 2 s result in an experimental time of 4 h and 40 min.

After Fourier transformation in the spatial dimensions, the diffusion tensors were estimated voxel-wise by non-linear least squares fitting of Eq. 13 with Eq. 12 to the experimental signal intensities using the initial signal intensity I_0, the eigenvalues λ_1, λ_2, and λ_3, as well as the three Euler angles as adjustable parameters. For display purposes, the diffusion tensors were represented as superquadrics [54] and the DTI indices MD, FA, CP, and CL were calculated using Eqs. 16–19.

The longitudinal and transverse relaxation times T_1 and T_2 are about 1 s and 30 ms, respectively, for the residual water protons in the $C_{10}E_3/^2H_2O$ mixture, giving some T_1- and T_2-weighting of the signal at the herein used recycle delay and echo time. The relaxation weighting affects the value of I_0 in Eq. 13, but should not alter the estimated diffusion tensors.

The quadrupolar echo pulse sequence in Fig. 2 (b) was used to record ^2H spectra with spatial resolution in three dimensions. Signal acquisition was initiated at the top of the quadrupolar echo occuring 4 ms after the initial 90° pulse. The signal was collected for 0.41 s with a spectral width of 2500 Hz and 2048 time domain points. With 0.2 s recycle delay and accumulation of 4 scans, the experimental time was 11 h and 22 min.

Fourier transformation along all four acquisition dimensions generated one ^2H spectrum per voxel. The individual ^2H spectra were processed with automatic phase and baseline correction. On account of our acquisition and processing protocol, including phase correction rather than the more common magnitude calculation, the voxel-resolved ^2H spectra have a quality that is comparable to what can be obtained with conventional ^2H spectroscopy without spatial resolution. The ^2H spectrum indices A, M_1, and M_2 were calculated using Eqs. 9–11. The fractional population of water in the MLVs, f_{MLV}, was estimated from the ^2H spectra $I(\nu)$ by non-linear least squares fitting of

$$I(\nu) = I_0[f_{MLV} I_{MLV}(\nu) + (1 - f_{MLV}) I_P(\nu)], \qquad (20)$$

where the spectrum from the MLVs, $I_{MLV}(\nu)$, and the powder pattern $I_P(\nu)$ are given by Eqs. 8 and 5, respectively. In the evaluation of Eq. 5, the probability distribution of domain orientations $P(\alpha)$ as expressed in Eq. 7 was used. The fitting was performed both with and without the constraint $f_{MLV} = 1$. If there

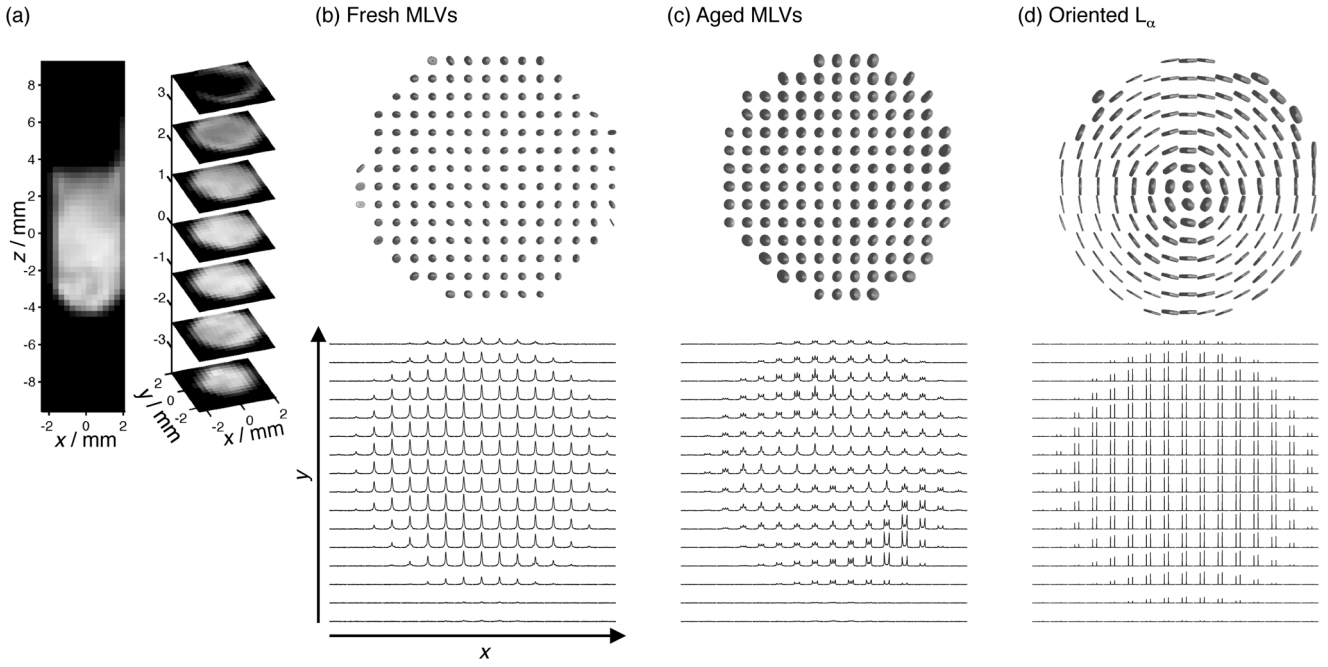

Figure 3. Representative DTI and ^2H data for $C_{10}E_3$/water lamellar phases. (a) Selected 2D slices from a conventional T_2-weighted ^1H 3D image for a freshly prepared sample of multi-lamellar vesicles (MLVs). (b), (c), and (d): 2D arrays of diffusion tensors (top) and ^2H spectra (bottom) for fresh MLVs, 12 days aged MLVs, and an oriented lamellar phase L_α obtained by 36 days equilibration after a temperature quench. The 2D arrays show the $z = 0$ slices extracted from the full data sets with spatial resolution in three dimensions. Diffusion tensors are shown only for voxels with ^1H signal intensity significantly above the noise level.
doi:10.1371/journal.pone.0098752.g003

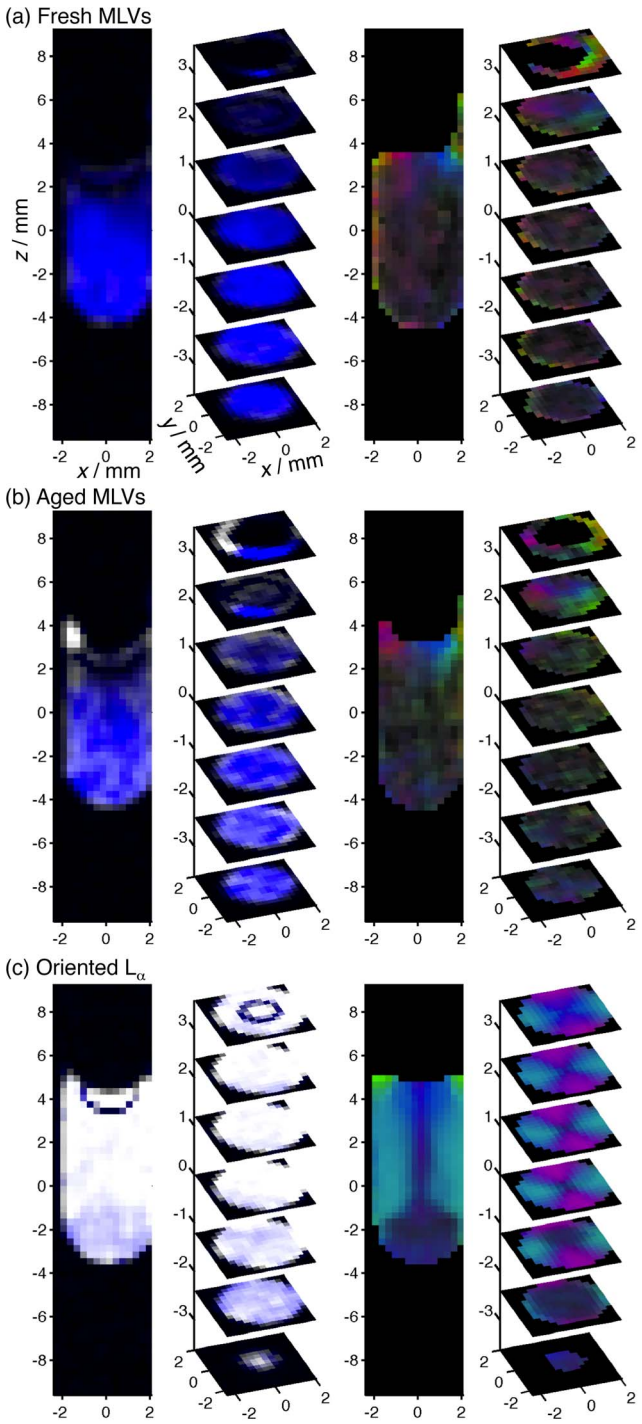

Figure 4. Color-coded ^{2}H NMR and DTI data with spatial resolution in 3D. ^{2}H NMR (left) and DTI (right) for $C_{10}E_3$/water lamellar phases with different superstructures: (a) fresh MLVs, (b) MLVs aged 12 days, (c) and oriented L_α equilibrated 36 days after a temperature quench. The voxels of the ^{2}H NMR data are color-coded with the ^{2}H peak area A (brightness) and second moment M_2 (narrow to broad peak: blue to white). The voxels of the DTI data are color-coded using RGB triplets calculated as FA·$[D_{xx}, D_{yy}, D_{zz}]/\lambda_1$.
doi:10.1371/journal.pone.0098752.g004

was no significant improvement of the fit quality by allowing f_{MLV} to vary, then f_{MLV} was set to unity.

While the values of T_1 and T_2 are approximately 0.5 s for pure ^2H_2O, they could be considerably smaller and differ between the various lamellar morphologies, possibly leading to systematic errors in the estimated values of f_{MLV}. The relaxation weighting should be taken into account if the value of f_{MLV} is in itself the parameter of interest, but it is of minor importance for the current study where we infer the rate of MLV breakdown from the change of f_{MLV} as a function of time.

Results and Discussion

Reference lamellar morphologies

Fig. 3 shows DTI and ^{2}H data for three representative $C_{10}E_3$/water lamellar phases with identical bulk chemical composition and temperature, but different morphology on length scales above micrometers because of sample history. The overall shape of the sample is visible in the standard ^{1}H image in (a), which also shows the $z=0$ slice that is investigated in more detail in panels (b)-(d). Information about the sub-voxel morphology can be obtained by comparing the diffusion tensors and ^{2}H spectra with the schematic data in Fig. 1.

The experimental data for the freshly prepared MLV sample agree well with the isotropic diffusion tensor and the broad ^{2}H singlet shown for case (h) in Fig. 1. Visual inspection of the 2D arrays of diffusion tensors and ^{2}H spectra in Fig. 1 (b) verify that the sample is nearly homogeneous. A few diffusion tensors with markedly flat shape are visible at the left-most voxels, possibly indicating the presence of a uniformly oriented lamellar phase, but more likely resulting from a failure of the DTI fitting process on account of the rather low signal intensity in these voxels. Still, careful inspection of the ^{2}H spectra reveals low-amplitude doublets in the immediate vicinity of the container walls, indicating that the MLVs have started to transform into other morphologies. When using standard ^{2}H spectroscopy without spatial resolution, there is no trace of other morphologies than the MLVs (data not shown).

The transformation of the MLVs is apparent in the data for the aged MLV sample in panel Fig. 3 (c). The ^{2}H spectra show the presence of voxels with almost pure MLVs (single broad peak), as well as some voxels with seemingly uniformly oriented lamellar phase (doublet without "shoulders"). Voxel-by-voxel comparison with the diffusion tensors shows that the domain orientation is not completely uniform even in the voxels with the sharpest ^{2}H doublets. As a reference for this observation, we can use the data for the highly oriented lamellar phase in panel (d). All voxels show ^{2}H spectra with doublets having just a small fraction of the linewidth of the sharpest doublets in panel (c). Analogously, the

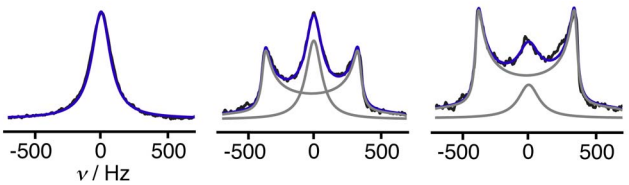

Figure 5. Estimation of the fraction of MLVs (f_{MLV}) by spectral deconvolution of ^{2}H data. The observed spectrum is the sum of contributions from MLVs (singlet) and other lamellar morphologies (doublet). Experimental, fitted, and deconvoluted ^{2}H spectra are shown with black, blue, and gray lines, respectively. The deconvolution process yields the values $f_{MLV}=1$, 0.32, and 0.14 from left to right.
doi:10.1371/journal.pone.0098752.g005

diffusion tensors are flat, with values of the planar index CP approaching unity. Comparison to the schematic data in Fig. 1 shows that the lamellae are uniformly oriented within each voxel, and that the directors lie in the *xy*-plane, pointing radially with respect to the axis of the sample tube. The diffusion tensors in the very center of the tube are cylindrical rather than planar, indicating that these voxels contain domains with directors spread out in the *xy*-plane, corresponding to case (d) in Fig. 1.

In order to facilitate graphical display of the 3D data, some useful indices are extracted from the ^{2}H spectra and diffusion tensors, and shown as color-coded images in Fig. 4. The brightness of the ^{2}H images is proportional to the total ^{2}H peak area A within each voxel, while the color-scale (from blue to white) corresponds to the ^{2}H peak width expressed as the second moment of the linewidth M_2. Intensely blue voxels thus show the presence of MLVs, while white voxels signify oriented lamellar phase. The black band below the meniscus is caused by the difference in magnetic susceptibility between the sample and the surrounding air, leading to inhomogeneity in the magnetic field and signal loss that cannot be refocused with the quadrupolar echo sequence. The DTI data is color-coded using RGB triplets calculated as [R, G, B] = FA·$[D_{xx}, D_{yy}, D_{zz}]/\lambda_1$. Consequently, the brightness is given by FA while the color gives visual cues for the shapes and orientations of the tensors. The purple and turquoise colors in panel (c) originate from diffusion tensors with $D_{xx} = D_{zz} \gg D_{yy} = 0$ and $D_{yy} = D_{zz} \gg D_{xx} = 0$, respectively, signifying diffusion tensors with planar shape, i.e. CP = 1, and uniformly oriented lamellar domains within each voxel.

The color-coded ^{2}H data in Fig. 4 is consistent with direct inspection of the ^{2}H spectra in Fig. 3. The rather homogeneous blue and white colors in panels (a) and (c) correspond to homogeneous samples with MLVs and oriented L_α, respectively. The pattern with blue tint in panel (b) shows the regions where the MLVs have partially transformed to other morphologies. The difference between the fresh and the aged MLV samples is less apparent in the DTI data, which however is quite powerful for showing the director orientations in the oriented L_α in panel (c). The director is located radially with respect to the tube axis, with the exception of the very bottom of the tube. In this particular region, which is also visible as a weak blue tint in the color-coded ^{2}H data, the ^{2}H spectra feature sharp doublets, but with a few percent smaller splitting than in the rest of the sample. Tentatively, we attribute this observation to a small difference in chemical composition that remains even a month after the sample was

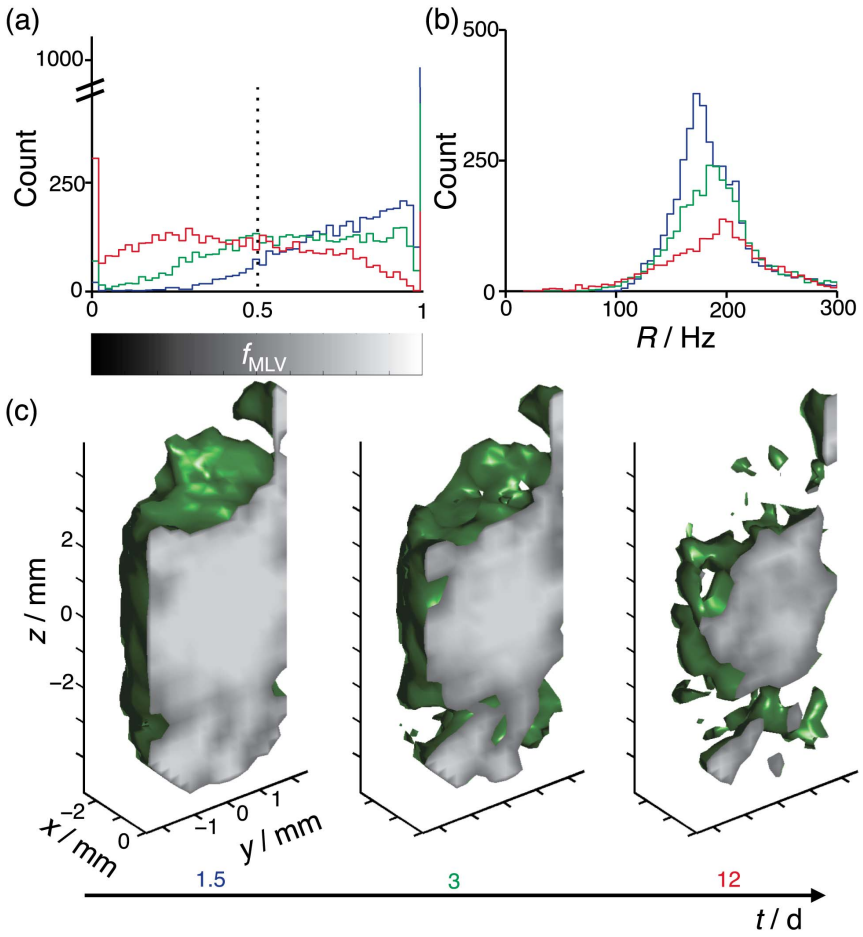

Figure 6. Time-resolved 3D mapping of the breakdown of MLVs to other lamellar morphologies. Spectral deconvolution of spatially resolved ^{2}H NMR spectra gives estimates of the fraction of MLVs f_{MLV} and peak width R of the MLV singlet. Histograms of f_{MLV} and R are shown in panels (a) and (b), respectively, for the times $t = 1.5$ (blue), 3 (green) and 12 (red) days after MLV preparation. The dashed line in (a) indicates the value used for separating between voxels dominated by MLVs ($f_{MLV} > 0.5$) or other lamellar morphologies ($f_{MLV} < 0.5$). The counts in (b) are weighted by the values of f_{MLV}. (c) 3D rendering of the contour $f_{MLV} = 0.5$ (green surface) at the times $t = 1.5$, 3 and 12 days. The surface at $x = 0$ represents f_{MLV} with gray scale given by the bar on the f_{MLV}-axis in panel (a).
doi:10.1371/journal.pone.0098752.g006

quenched from the high-temperature phase-separated state with pure water in the bottom of the tube.

Breakdown of multi-lamellar vesicles

In the presence of the externally applied shear field, the MLV phase is the thermodynamic equilibrium structure [61]. After turning off the shear, there is a thermodynamic tendency for a phase transition to the new equilibrium structure, i.e. a lamellar phase with flat rather than curved surfactant bilayers. Although the MLV phase is metastable for days, allowing for detailed investigation using techniques that are not compatible with the application of shear, the data in Figs. 3 and 4 show that the MLVs transform on the time scale of days, and that the transformation is spatially inhomogeneous.

In order to put these observation on a more quantitative basis, we use voxel-resolved estimates of the fraction of water residing in MLVs, f_{MLV}, to segment the 3D images into regions that are dominated by either MLVs or other lamellar phase morphologies. The values of f_{MLV} are obtained by deconvolution of the ^2H spectrum in each voxel, and Fig. 5 shows examples of the deconvolution process for three representative voxels extracted from the full 3D ^2H spectroscopic imaging data obtained on an aged MLV sample. The broad singlet at 0 Hz arises from the MLVs, whereas the powder-pattern doublet with maxima at ± 400 Hz originates from randomly orientated domains of lamellar phase.

The histograms in Fig. 6 represent the temporal change of f_{MLV} and width R of the MLV singlet. The shift of the f_{MLV}-distribution towards smaller values reflects the breakdown of the MLVs with time. When constructing the R-distributions, the contribution from each voxel was weighed by its value of f_{MLV}, thus reducing the influence from voxels with low amplitude of the MLV peak. Consequently, the distributions are to a reasonable approximation weighted by the mass of water. With time, the main effect on the R-distribution is a decreasing amplitude on account of the decreasing values of f_{MLV}, but also a shift of the maximum from 180 to 200 Hz, corresponding to a 5% increase in size according to the proportionality between R and the square of the MLV size [24,44]. From these observations we conclude that the MLVs decrease in number while having a fairly constant size distribution.

The spatial pattern of the MLV breakdown is monitored by selecting voxels having f_{MLV} above 0.5. This threshold value is displayed as a sequence of 3D contour surfaces in Fig. 6 (c). We wish to point out that both the spatial and the temporal changes of f_{MLV} are always smooth, meaning that the surfaces in Fig. 6 (c) should be interpreted simply as a contour in the smoothly varying f_{MLV} data rather than as a sharp interface between MLVs and other types of lamellar phases. The transition initially takes place close to the tube walls and then gradually progresses through the sample volume. Although the bulk of the sample has transformed, there are still isolated islands with pristine MLVs nearly two weeks after sample preparation.

The kinetics of phase transitions are often described by the Johnson-Mehl-Avrami-Kolmogorov (JMAK) model [45,62–64], which has previously been applied to nonionic surfactant systems [46]. In the current context, we write the JMAK-model as

$$f_{MLV} = \exp(-kt^{\beta}), \tag{21}$$

where t is the time, k is the rate constant, and β is the so-called Avrami constant. The half-life time τ of the non-equilibrium phase is calculated by

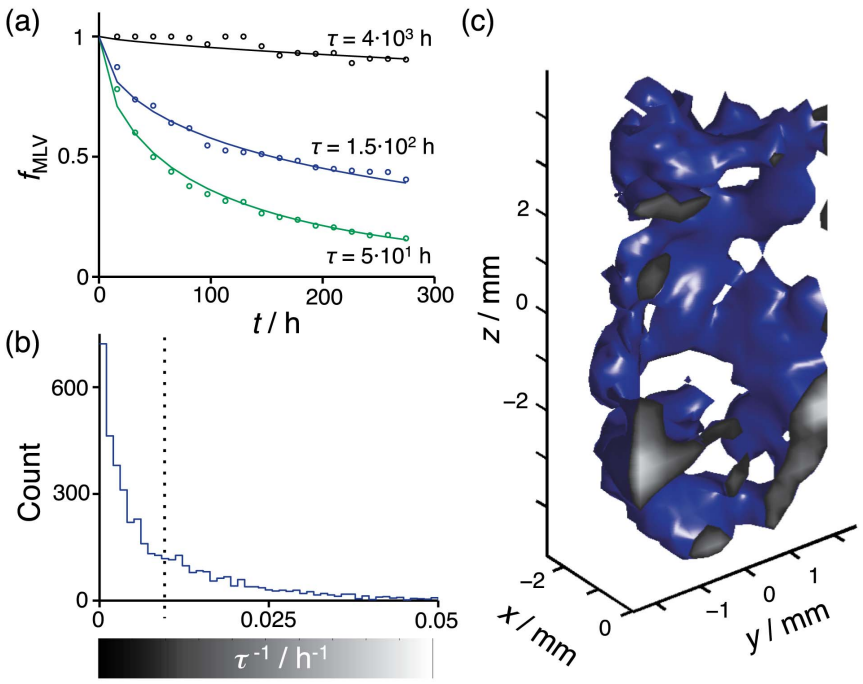

Figure 7. JMAK analysis of the transition from MLVs to a lamellar phase. (a) Fraction of MLVs f_{MLV} vs. time t for the entire sampe (blue) and two individual voxels (black and green). Fitting Eq. 21 (lines) to the experimental data (circles) gives estimates of the half-life time τ. (b) Histogram of τ^{-1} with the dashed line indicating the cut-off value used for separating between voxels with fast ($\tau^{-1} > 0.01$ h^{-1}) and slow ($\tau^{-1} < 0.01$ h^{-1}) breakdown of the MLVs. (c) 3D rendering of the $\tau^{-1} = 0.01$ h^{-1} contour (blue surface). The surface at $x = 0$ shows the values of τ^{-1} according to the gray-scale bar in (b).
doi:10.1371/journal.pone.0098752.g007

$$\tau = \left[\frac{\ln(2)}{k}\right]^{\frac{1}{\beta}}. \quad (22)$$

Conventionally, the JMAK model is applied to the total phase composition in bulk samples. Each voxel of the 3D image has a volume of 30 nL and initially contains on the order of 10^6 MLVs, and can thus be treated as an individual sample giving spatially resolved values of τ. The JMAK model describes the experimental data well as shown for representative voxels in Fig. 7 (a). The voxels are chosen to illustrate the many orders of magnitude spread in the values of τ, from 50 to at least $4{\cdot}10^3$ h. The upper limit of τ is difficult to determine since the experiment was terminated after 300 h.

Fig. 7 (b) shows a histogram of $1/\tau$, revealing a continuous distribution of breakdown rates. A $1/\tau$ threshold value of 0.01 h^{-1}, which splits the distribution into two halves with approximately equal areas, was chosen to discriminate between voxels with short- and long-lived MLVs. This threshold value is rendered as a 3D surface in Fig. 7 (c), showing that there is a tendency for voxels with short-lived MLVs to be located in the vicinity of the tube walls.

A phase transition involving a nucleation-and-growth mechanism with only a few separated nucleation sites would presumably lead to some voxels displaying an initial lag time, without changes in f_{MLV}, before the onset of a rapid phase transition as the equilibrium phase grows from the nucleation sites and eats its way into the rest of the sample. Voxels with such behavior could not be found, thus indicating that the MLVs transform with a rate that is given by the initial conditions within the voxel. Further discussions on the phase transition mechanism is beyond the scope of this paper, but we wish to emphasize that our experimental approach gives highly detailed data that could be used to test models for the mechanisms.

Alignment of a lamellar phase

As a final example, we show the transition between randomly and uniformly oriented lamellar phases. The experiment was performed on a sample that was initially phase separated at 67°C into a reverse micellar phase (top) and pure water (bottom), both of which are isotropic. After a temperature quench to 25°C,

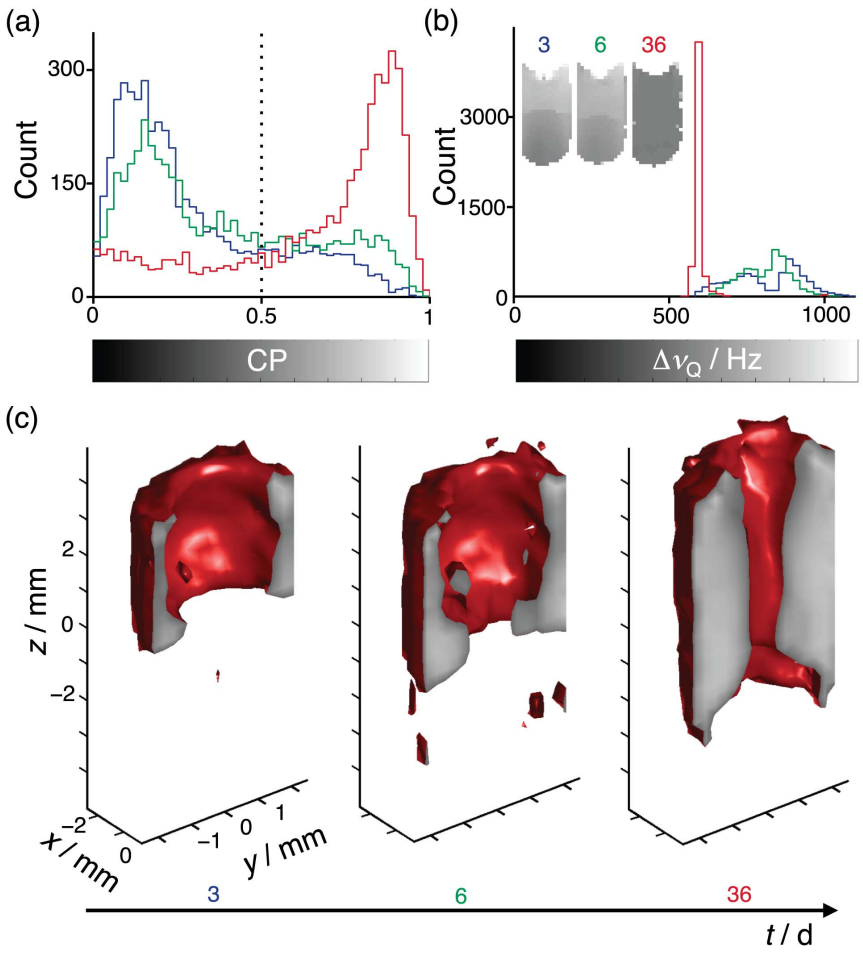

Figure 8. Time-resolved 3D mapping of the formation of a macroscopically oriented lamellar phase. Panels (a) and (b) show histograms of the planar diffusion anisotropy index CP and the ^{2}H quadrupolar splitting $\Delta\nu_Q$ at the times $t =$ 3 (blue), 6 (green), and 36 (red) days after a temperature quench from 67 to 25°C. The vertical dashed line in (a) indicates the value of CP for segmenting the 3D image into oriented (CP >0.5) and non-oriented (CP <0.5) lamellar phase. Insets in (b) show $\Delta\nu_Q$ maps at $x=0$, gray-scale coded according to the bar below the $\Delta\nu_Q$-axis. (c) 3D rendering of the CP$=0.5$ contour (red surface) for the times $t =$ 3, 6, and 36 days after the temperature quench. The surface at $x=0$ indicates the value of CP according to the gray-scale bar in (a).
doi:10.1371/journal.pone.0098752.g008

anisotropic phases form throughout the sample after approximately 1 day. At this time, the combination of information from the ^{2}H and DTI data shows that lamellar phases of various morphologies have formed throughout the sample despite the fact that there is still a gradient in chemical composition along the z-axis.

Histograms of the planar index CP and the ^{2}H quadrupolar splitting $\Delta\nu_Q$ are displayed in Fig. 8 (a) and (b), respectively. Values of CP approaching unity indicate the presence of uniformly oriented lamellar phases, whereas $\Delta\nu_Q$ is proportional to surfactant-to-water ratio [41,44]. The insets in (b) show $\Delta\nu_Q$ maps, revealing an initially heterogeneous sample composition that gradually becomes homogeneous. The CP distributions have significant amplitude over the entire range from 0 to 1, but also well-defined maxima at 0.1 and almost 1. The spatial distribution of the oriented lamellar phase is mapped by segmenting the 3D image using the threshold value $CP = 0.5$. As opposed to the case with the MLVs discussed above, there is a distinct step in CP between voxels with uniformly and randomly oriented lamellar phases, resulting in a sharp and well-defined interface between the two morphologies.

The gradual formation of an oriented lamellar phase is illustrated by the sequence of 3D images in Fig. 8 (c). Initially, the oriented phase forms at the container walls in the top region of the sample where the surfactant concentration is highest. With time, the ordered phase grows downwards along the walls of the tube, and inwards towards the center of the tube. In the time period between 7 and 35 days after the temperature quench, the sample was stored far from the strong magnetic field of the NMR magnet. Still, the oriented phase kept on growing, finally filling the major part of the tube. From this observation we conclude that interaction with the glass walls of the tube is the main factor for the alignment of the $C_{10}E_3$/water lamellar phase.

Conclusions

The experimental results presented in this paper show that the combination of data from 3D diffusion tensor and ^{2}H spectroscopic imaging yields a wealth of information on the morphology of liquid crystalline structures on a range of length scales. The combination of methods is necessary since they by themselves fail to distinguish between certain morphologies, e.g., MLVs and randomly oriented lamellar phases for DTI, as well as uniformly and 2D randomly oriented lamellar phases for ^{2}H. Image segmentation based on appropriately chosen scalar parameters and confirmed by voxel-by-voxel visual inspection of diffusion tensors and ^{2}H spectra allow for time-resolved 3D mapping of the spatial distribution of lamellar morphologies during phase transitions and subsequent equilibration. The combination of methods may prove to be useful in fundamental studies of phase transition mechanisms and for characterization of tailor-made metastable morphologies being produced by, e.g., temperature cycling or the application of external fields. The current implementation of the measurement protocol is limited to samples that remain stable on the time-scale of tens of hours, but we expect that the time resolution could be greatly improved by compressed sensing approaches with sparse sampling of the acquisition dimensions [65].

Acknowledgments

Magnus Röding is acknowledged for valuable discussions and careful reading of the manuscript.

Author Contributions

Conceived and designed the experiments: DB VK MN DT. Performed the experiments: DB VK DT. Analyzed the data: DB DT. Contributed reagents/materials/analysis tools: VK DT. Wrote the paper: DB VK MN DT.

References

1. Evans DF, Wennerström H (1999) The colloidal domain: where physics, chemistry, biology and technology meet. 2nd ed. New York: Wiley VCH. 672 p.
2. Jonsson B, Holmberg K, Kronberg B, Lindman B (2002) Surfactants and polymers in aqueous solution. Chichester: John Wiley & Sons, Ltd. 547 p.
3. Iwashita Y, Tanaka H (2006) Self-organization in phase separation of a lyotropic liquid crystal into cellular, network and droplet morphologies. Nat Mater 5: 147–152.
4. Briganti G, Segre AL, Capitani D, Casieri C, La Mesa C (1999) Isooriented lyotropic lamellar phase in the $C_{12}E_6/D_2O$ system. J Phys Chem B 103: 825–830.
5. Yethiraj A, Capitani D, Burlinson NE, Burnell EE (2005) An NMR study of translational diffusion and structural anisotropy in magnetically alignable nonionic surfactant mesophases. Langmuir 21: 3311–3321.
6. Capitani D, Casieri C, Briganti G, La Mesa C, Segre AL (1999) Phase diagram of the $C_{12}E_6/D_2O$ system revisited: Effect of strong magnetic fields. J Phys Chem B 103: 6088–6095.
7. Capitani D, Yethiraj A, Burnell EE (2007) Memory effects across surfactant mesophases. Langmuir 23: 3036–3048.
8. Zipfel J, Nettesheim F, Lindner P, Le TD, Olsson U, et al. (2001) Cylindrical intermediates in a shear-induced lamellar-to-vesicle transition. Europhys Lett 53: 335–341.
9. Nettesheim F, Zipfel J, Olsson U, Renth F, Lindner P, et al. (2003) Pathway of the shear-induced transition between planar lamellae and multilamellar vesicles as studied by time-resolved scattering techniques. Langmuir 19: 3603–3618.
10. Pommella A, Caserta S, Guida V, Guido S (2012) Shear-induced deformation of surfactant multilamellar vesicles. Phys Rev Lett 108: 138301–138304.
11. Redkar M, Hassan PA, Aswal V, Devarajan P (2007) Onion phases of PEG-8 distearate. J Pharm Sci 96: 2436–2445.
12. Rosedale JH, Bates FS (1990) Rheology of ordered and disordered symmetric poly(ethylenepropylene) poly(ethylethylene) diblock copolymers. Macromolecules 23: 2329–2338.
13. Oliviero C, Coppola L, Gianferri R, Nicotera I, Olsson U (2003) Dynamic phase diagram and onion formation in the system $C_{10}E_3/D_2O$. Colloids Surf, A 228: 85–90.
14. Le TD, Olsson U, Mortensen K, Zipfel J, Richtering W (2001) Nonionic amphiphilic bilayer structures under shear. Langmuir 17: 999–1008.
15. Gauffre F, Roux D (1999) Studying a new type of surfactant aggregate (''spherulites'') as chemical microreactors. a first example: Copper ion entrapping and particle synthesis. Langmuir 15: 3738–3747.
16. Freund O, Amedee J, Roux D, Laversanne R (2000) In vitro and in vivo stability of new multilamellar vesicles. Life Sci 67: 411–419.
17. Attard GS, Glyde JC, Göltner CG (1995) Liquid-crystalline phases as templates for the synthesis of mesoporous silica. Nature 378: 366–368.
18. Squires AM, Hallett JE, Beddoes CM, Plivelic TS, Seddon AM (2013) Preparation of films of a highly aligned lipid cubic phase. Langmuir 29: 1726–1731.
19. Levitt MH (2008) Spin dynamics: Basics of nuclear magnetic resonance. 2nd ed. Chichester: John Wiley & Sons, Ltd. 744 p.
20. Khan A, Fontell K, Lindblom G, Lindman B (1982) Liquid crystallinity in a calcium surfactant system - phase-equilibria and phase structures in the system calcium octyl sulfate decan-1-ol water. J Phys Chem 86: 4266–4271.
21. Khan A, Fontell K, Lindblom G (1982) Phase-equilibria of the system hexadecyltrimethylammonium fluoride-water studied by ^{2}H, ^{14}N, and ^{19}F nuclear magnetic resonance. J Chem Phys 86: 383–386.
22. Brown JR, Callaghan PT (2011) Changing micellar order, lever rule behavior and spatio-temporal dynamics in shear-banding at the onset of the stress plateau. Soft Matter 7: 10472–10482.
23. Medronho B, Shafaei S, Szopko R, Miguel MG, Olsson U, et al. (2008) Shear-induced transitions between a planar lamellar phase and multilamellar vesicles: Continuous versus discontinuous transformation. Langmuir 24: 6480–6486.
24. Medronho B, Schmidt C, Olsson U, Miguel MG (2010) Size determination of shear-induced multilamellar vesicles by rheo-NMR spectroscopy. Langmuir 26: 1477–1481.
25. Dvinskikh SV, Furo I (2001) Domain structure in an unoriented lamellar lyotropic liquid crystal phase studied by ^{2}H NMR. Langmuir 17: 6455–6460.
26. Medronho B, Olsson U, Schmidt C, Galvosas P (2012) Transient and steady-state shear banding in a lamellar phase as studied by rheo-NMR. Z Phys Chem 226: 1293–1314.

27. Stejskal EO (1965) Use of spin echoes in a pulsed magnetic-field gradient to study anisotropic restricted diffusion and flow. J Chem Phys 43: 3597.
28. Price WS (2009) NMR studies of translational motion: Principles and Applications. New York: Cambridge University Press. 416 p.
29. Callaghan PT (2011) Translational dynamics & magnetic resonance. USA: Oxford University Press. 576 p.
30. Callaghan PT, Söderman O (1983) Examination of the lamellar phase of Aerosol OT-water using pulsed field gradient nuclear magnetic resonance. J Phys Chem 87: 1737–1744.
31. Topgaard D, Söderman O (2002) Self-diffusion in two- and three-dimensional powders of anisotropic domains: An NMR study of the diffusion of water in cellulose and starch. J Phys Chem B 106: 11887–11892.
32. Åslund I, Cabaleiro-Lago C, Söderman O, Topgaard D (2008) Diffusion NMR for determining the homogeneous length-scale in lamellar phases. J Phys Chem B 112: 2782–2794.
33. Åslund I, Medronho B, Topgaard D, Söderman O, Schmidt C (2011) Homogeneous length scale of shear-induced multilamellar vesicles studied by diffusion NMR. J Magn Reson 209: 291–299.
34. Basser PJ, Mattiello J, Le Bihan D (1994) MR diffusion tensor spectroscopy and imaging. Biophys J 66: 259–267.
35. Basser PJ, Mattiello J, Le Bihan D (1994) Estimation of the effective self-diffusion tensor from the NMR spin-echo. J Magn Reson 103: 247–254.
36. Klinkenberg M, Blümler P, Blümich B (1996) ^{2}H NMR imaging of strained elastomers. J Magn Reson A 119: 197–203.
37. Le Bihan D, Breton E, Lallemand D, Grenier P, Cabanis E, et al. (1986) MR imaging of intravoxel incoherent motions - application to diffusion and perfusion in neurologic disorders. Radiology 161: 401–407.
38. Callaghan PT, Eccles CD, Xia Y (1988) NMR microscopy of dynamic displacements - k-space and q-space imaging. J Phys E 21: 820–822.
39. Fischer E, Callaghan PT (2000) Is a birefringence band a shear band? Europhys Lett 50: 803–809.
40. Medronho B, Brown J, Miguel MG, Schmidt C, Olsson U, et al. (2011) Planar lamellae and onions: a spatially resolved rheo-NMR approach to the shear-induced structural transformations in a surfactant model system. Soft Matter 7: 4938–4947.
41. Bulut S, Åslund I, Topgaard D, Wennerström H, Olsson U (2010) Lamellar phase separation in a centrifugal field. A method for measuring interbilayer forces. Soft Matter 6: 4520–4527.
42. Szutkowski K, Jurga S (2010) Long-range ordering in the lyotropic lamellar phase studied by high-resolution magnetic resonance diffusion-weighted imaging. J Phys Chem B 114: 165–173.
43. Lasič S, Szczepankiewicz F, Eriksson S, Nilsson M, Topgaard D (2014) Microanisotropy imaging: quantification of microscopic diffusion anisotropy and orientational order parameter by diffusion MRI with magic-angle spinning of the q-vector. Front Phys 2: 1–14.
44. Ferreira TM, Bernin D, Topgaard D (2013) NMR studies of nonionic surfactants. Annu Rep NMR Spectrosc 79: 73–127.
45. Fanfoni M, Tomellini M (1998) The Johnson-Mehl-Avrami-Kolmogorov model: A brief review. Nuovo Cimento Soc Ital Fis, D 20: 1171–1182.
46. Gotter M, Strey R, Olsson U,Wennerström H (2005) Fusion and fission of fluid amphiphilic bilayers. Faraday Discuss 129: 327–338.
47. Harris RK (1983) Nuclear magnetic resonance spectroscopy: A physicochemical view. Harlow: Longman. 282 p.
48. Davis JH (1983) The description of membrane lipid conformation, order and dynamics by 2H-NMR. Biochim Biophys Acta 737: 117–171.
49. Struis RPWJ, de Bleijser J, Leyte JC (1987) Dynamic behavior and some of the molecular properties of water molecules in pure water and in $MgCl_2$ solutions. J Phys Chem 91: 1639–1645.
50. Hubbard PL, McGrath KM, Callaghan PT (2006) Evolution of a lamellar domain structure for an equilibrating lyotropic liquid crystal. J Phys Chem B 110: 20781–20788.
51. Kingsley PB (2006) Introduction to diffusion tensor imaging mathematics: Part I. Tensors, rotations, and eigenvectors. Concepts Magn Reson, Part A 28: 101–122.
52. Kingsley PB (2006) Introduction to diffusion tensor imaging mathematics: Part III. Tensor calculation, noise, simulations, and optimization. Concepts Magn Reson, Part A 28: 155–179.
53. Susumu M (2007) Introduction to diffusion tensor imaging. Oxford: Elsevier. 190 p.
54. Kindlmann G (2004) Superquadric tensor glyphs. In: Joint EUROGRAPHICS - IEEE TCVG Symposium on Visualization. Aire-la-Ville, Switzerland. p 147–154.
55. Basser PJ, Pierpaoli C (1996) Microstructural and physiological features of tissues elucidated by quantitative-diffusion-tensor MRI. J Magn Reson 111: 209–219.
56. Kingsley PB (2006) Introduction to diffusion tensor imaging mathematics: Part II. Anisotropy, diffusion-weighting factors, and gradient encoding schemes. Concepts Magn Reson, Part A 28: 123–154.
57. Westin CF, Peled S, Gudbjartsson H, Kikinis R, Jolesz FA (1997) Geometrical diffusion measures for MRI from tensor basis analysis. In: ISMRM '97. Vancouver Canada. p 1742.
58. Pake GE (1948) Nuclear resonance absorption in hydrated crystals - fine structure of the proton line. J Chem Phys 16: 327–336.
59. van Beek JD (2007) matNMR: A flexible toolbox for processing, analyzing and visualizing magnetic resonance data in Matlab. J Magn Reson 187: 19–26.
60. Chen L, Weng Z, Goh L, Garland M (2002) An efficient algorithm for automatic phase correction of NMR spectra based on entropy minimization. J Magn Reson 158: 164–168.
61. Medronho B, Miguel MG, Olsson U (2007) Viscoelasticity of a nonionic lamellar phase. Langmuir 23: 5270–5274.
62. Avrami M (1939) Kinetics of phase change. I. General theory. J Chem Phys 7: 1103–1112.
63. Avrami M (1941) Granulation, phase change, and microstructure - kinetics of phase change. III. J Chem Phys 9: 177–184.
64. Johnson WA, Mehl RF (1939) Reaction kinetics in processes of nucleation and growth. Trans Am Inst Min, Metall Pet Eng 135: 416–442.
65. Lustig M, Donoho D, Pauly JM (2007) Sparse MRI: The application of compressed sensing for rapid MR imaging. Magn Reson Med 58: 1182–1195.